Climate mitigation from vegetation biophysical feedbacks during the past three decades

Zhenzhong Zeng, Shilong Piao, Laurent Z. X. Li, Liming Zhou, Philippe Ciais, Tao Wang, Yue Li, Xu Lian, Eric F. Wood, Pierre Friedlingstein, et al.

Climate mitigation from vegetation biophysical feedbacks during the past three decades

Zhenzhong Zeng[1], Shilong Piao[1,2,3]*, Laurent Z. X. Li[4], Liming Zhou[5], Philippe Ciais[6], Tao Wang[2,3], Yue Li[1], Xu Lian[1], Eric F. Wood[7], Pierre Friedlingstein[8], Jiafu Mao[9], Lyndon D.Estes[7,10,11], Ranga B. Myneni[12], Shushi Peng[1], Xiaoying Shi[9], Sonia I. Seneviratne[13] and Yingping Wang[14]

[1]Sino-French Institute for Earth System Science, College of Urban and Environmental Sciences, Peking University, Beijing 100871, China
[2]Key Laboratory of Alpine Ecology and Biodiversity, Institute of Tibetan Plateau Research, Chinese Academy of Sciences, Beijing 100085, China
[3]Center for Excellence in Tibetan Earth Science, Chinese Academy of Sciences, Beijing 100085, China
[4]Laboratoire de Météorologie Dynamique, Centre National de la Recherche Scientifique, Sorbonne Universités, UPMC Univ Paris 06, 75252 Paris, France
[5]Department of Atmospheric and Environmental Sciences, University at Albany, State University of New York, Albany, New York 12222, USA
[6]Laboratoire des Sciences du Climat et de l'Environnement, UMR 1572 CEA-CNRS-UVSQ, 91191 Gif-sur-Yvette, France
[7]Department of Civil and Environmental Engineering, Princeton University, Princeton, New Jersey 08542, USA
[8]College of Engineering, Mathematics and Physical Sciences, University of Exeter, Exeter EX4 4QF, UK
[9]Environmental Sciences Division and Climate Change Science Institute, Oak Ridge National Laboratory, Oak Ridge, Tennessee 37831, USA
[10]Woodrow Wilson School, Princeton University, Princeton, New Jersey 08542, USA
[11]Graduate School of Geography, Clark University, Worcester, Massachusetts 01610, USA
[12]Department of Earth and Environment, Boston University, Boston, Massachusetts 02215, USA
[13]Institute for Atmospheric and Climate Science, Department of Environmental Systems Science, ETH Zurich, 8057 Zurich, Switzerland
[14]CSIRO Oceans and Atmosphere, PMB #1, Aspendale, Victoria 3195, Australia

The surface air temperature response to vegetation changes has been studied for the extreme case of land-cover change[1–5]; yet, it has never been quantified for the slow but persistent increase in leaf area index (LAI) observed over the past 30 years (Earth greening)[6,7]. Here we isolate the fingerprint of increasing LAI on surface air temperature using a coupled land–atmosphere global climate model prescribed with satellite LAI observations. We find that the global greening has slowed down the rise in global land-surface air temperature by 0.09±0.02℃ since 1982. This net cooling effect is the sum of cooling from increased evapotranspiration (70%), changed atmospheric circulation (44%), decreased shortwave transmissivity (21%), and warming from increased longwave air emissivity (-29%) and decreased albedo (-6%). The global cooling originated from the regions where LAI has increased, including boreal Eurasia, Europe, India, northwest Amazonia, and the Sahel. Increasing LAI did not, however, significantly change surface air temperature in eastern North America and East Asia, where the effects of large-scale atmospheric circulation changes mask local vegetation feedbacks. Overall, the sum of biophysical feedbacks related to the greening of the Earth mitigated 12% of global land-surfacewarming for the past 30 years.

Satellite data show unequivocally that the land surface has been greening for the past 30 years, and that leaf area index (LAI) has increased by 8% globally[6,7]. This satellite-observed greening of the Earth is supported by increased biomass from long-term forest inventories[8], model simulations[6,9] and observed enhancement of seasonal exchange of CO_2 (ref. 10). The increased photosynthetic removal of CO_2 from the atmosphere and consequent carbon sequestration potentially driven by this greening impose a negative forcing on the climate system[10,11]. Yet this negative forcing from the mitigation of atmospheric CO_2 growth could be enhanced or diminished by various biophysical feedbacks[1–5,12–15]. The biophysical feedbacks are largely controlled by LAI, a variable that regulates the amount of absorbed solar radiation by modifying albedo and the magnitude of evapotranspiration through canopy resistance[16]. The opposing effects of increased evapotranspiration (cooling) and decreased albedo (warming) for a given increase of LAI (refs 11,15), and further feedbacks through changes in cloud cover[17], atmospheric circulation and water recycling[18], make unravelling the fingerprint of the greening of the Earth on climate a major challenge in climate research.

Biophysical feedbacks are reasonably well studied for the vegetation variations associated with land-use/land-cover change[1–5]. Previous studies demonstrated that tropical afforestation attenuates warming locally through increasing evapotranspiration, whereas boreal afforestation exacerbates warming through decreasing albedo[14]. In particular, the Fifth Assessment Report (AR5) of the United Nations Intergovernmental Panel on Climate Change (IPCC) has evaluated the radiative forcing of land-surface changes only from the perspective of surface albedo ($-0.15 \pm 0.10\,W\,m^{-2}$; ref. 1). However, biophysical feedbacks of the observed widespread greening of the Earth during the past three decades[6,7] have not been examined to date. Here we quantify the response of land-surface air temperature to this greening during the past 30 years using a coupled land–atmosphere global climate model (GCM). To separate the effects of vegetation biophysical feedbacks from internal variability of the coupled climate system, we performed four simulations using the IPSLCM GCM (ref. 19) prescribed with different observed LAI and ocean sea-surface temperature (SST) distributions (see Supplementary Table 1 and Methods).

In experiment (1) the differences between simulations, LAIobs_OCNobs and LAIclim_OCNobs, isolate the fingerprint of observed LAI changes (referred to as ΔLAI) on climate (see Methods for details). Figure 1a shows the ΔLAI-induced global-mean change in land-surface 2-m air temperature (T_a), derived from the difference between the two simulations. In response to the greening, T_a significantly decreased at a rate of $-0.030 \pm 0.006\,^{\circ}C$ per decade ($p < 0.001$) along with the increase of LAI ($0.04 \pm 0.01\,m^2\,m^{-2}$ per decade, $p < 0.001$). This trend is very robust in the case of excluding the influence of significant

year-to-year variations in the modelled T_a (red lines in Fig. 1a). It is also robust in experiment (2) with LAIobs_OCNclim, where the satellite-observed LAI is the only year-to-year varying forcing, with an identical T_a trend of -0.030 ± 0.007 °C per decade ($p < 0.001$; Supplementary Fig. 1). Overall, at the global scale, the magnitude of the ΔLAI-induced cooling has been 0.09 ± 0.02 °C for the past 30 years—equivalent to 12% of the observed global land-surface warming of 0.89 °C over this period[20].

Physically, the change in T_a (referred to as ΔT_a) in response to ΔLAI can be decomposed into

$$\Delta T_a = \frac{1}{f}(-S\tau\Delta\alpha - \lambda\Delta E + S(1-\alpha)\Delta\tau + \varepsilon_s\sigma T_a^4\Delta\varepsilon_a + \frac{\rho C_d(T_s - T_a)}{r_a^2}\Delta r_a) + \Delta T_a^{cir} \quad (1)$$

where f is an energy redistribution factor, S is the solar radiation at the top of atmosphere, τ is the atmospheric shortwave transmissivity (that is, the proportion of extra-terrestrial solar radiation reaching the land surface), α is the surface albedo, λ is the latent heat of vaporization, E is the mass flux of water vapour (that is, evapotranspiration), ε_a is the near-surface air emissivity, T_s is the surface temperature, r_a is the aerodynamic resistance, and the residual term ΔT_a^{cir} is the influence of atmospheric circulation (details see Methods). The first five terms on the right attribute the response of T_a to the changes in α, E, τ, ε_a and r_a, respectively. Next, we discuss the individual contributions of each term to the temperature change.

It is well understood that increasing LAI reduces surface albedo but augments aerodynamic resistance and evapotranspiration[16]. Model results show that the observed variation in LAI over the past 30 years produces a decreasing trend in surface albedo ($-1.3 \pm 0.6 \times 10^{-4}$ per decade, $p < 0.05$; Supplementary Fig. 2a). For climatological values of S and τ, the decreasing albedo trend imposes a 0.03 ± 0.01 W m^{-2} per decade positive climate forcing over land ($-S\tau\Delta\alpha$ in equation (1); Fig. 1b). Aerodynamic resistance increases with LAI by 0.11 ± 0.06 s m^{-1} per decade ($p = 0.06$; Supplementary Fig. 2e), and imposes a negligible climate forcing (Fig. 1b). At the same time, the increasing LAI during the growing season leads to an increase in evapotranspiration of 0.32 ± 0.07 mm month^{-1} per decade ($p < 0.001$; Supplementary Fig. 2b). Shown as $-\lambda\Delta E$ in equation (1), this increase of evapotranspiration dissipates more land-surface absorbed energy and imposes a negative trend of climate forcing at the surface[12], the magnitude of which is -0.31 ± 0.07 W m^{-2} per decade ($p < 0.001$; Fig. 1b).

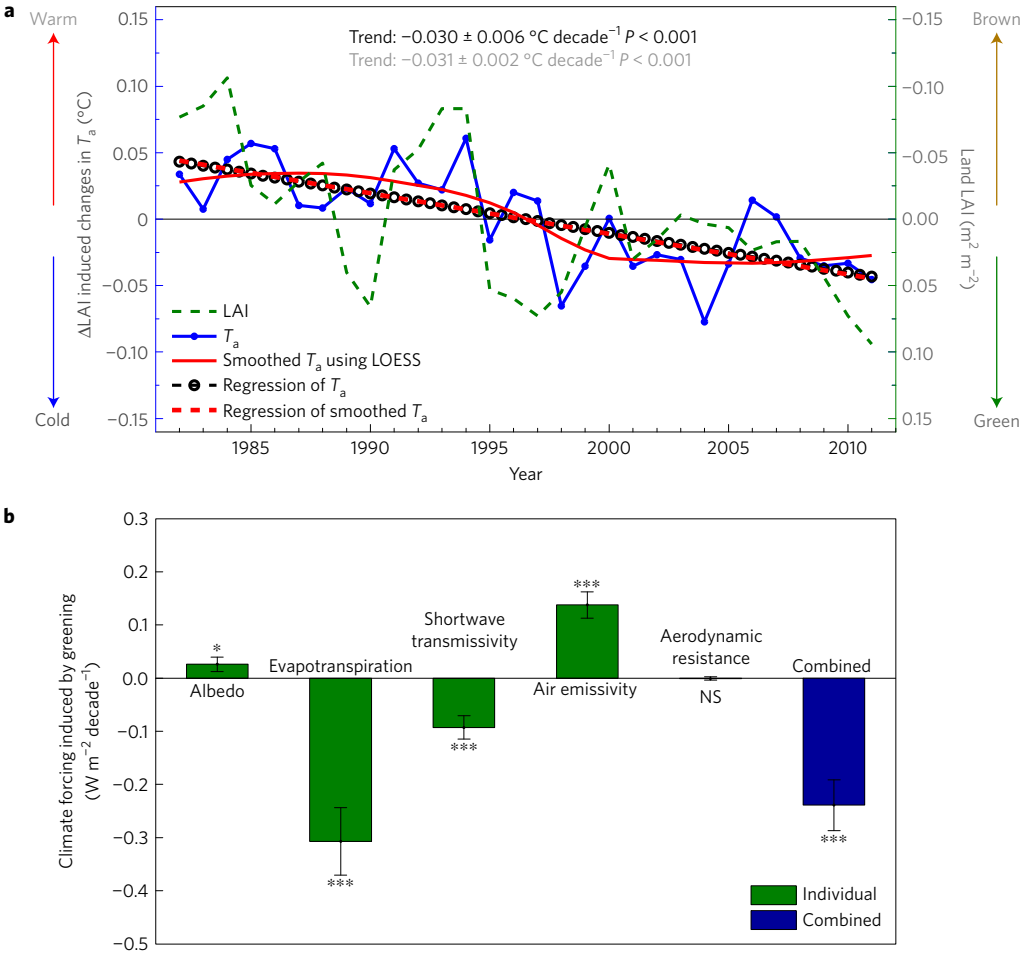

Figure 1 - ÎLAI-induced trends in annual average land-surface air temperature (T_a). a, Temporal variation of global land average LAI (green dotted line) and ΔLAI-induced variation in T_a (blue solid line) from experiment (1). The black straight line is the least squares regression of T_a against time. The red curve is the smoothed ΔLAI-induced variation in T_a using LOESS local regression with a default span value 0.75, and the red straight line is its regression. **b**, ΔLAI-induced trends in surface radiative forcing over the land surface associated with the changes in surface albedo ($-S\tau\Delta\alpha$), evapotranspiration ($-\lambda\Delta E$), shortwave transmissivity ($S(1-\alpha)\Delta\tau$), air emissivity ($\varepsilon_s\sigma T_a^4\Delta\varepsilon_a$) and aerodynamic resistance ($((\rho C_d(T_s - T_a))/r_a^2)\Delta r_a$) from experiment (1)(green bars). The blue bar is the sum of all surface radiative forcing. The significance of the trends are as follows: ***Significance at the 99% confidence interval; **Significance at the 95% confidence interval; *Significance at the 90% confidence interval.

The greening increases the evapotranspiration input of water vapour into the atmosphere, which in turn produces a series of indirect effects on the climate system[21]. On the one hand, the increased evapotranspiration to the atmosphere induces a negative trend of shortwave transmissivity of $-3.5 \pm 0.8 \times 10^{-4}$ per decade through the changes in clouds and water vapour content ($p < 0.001$; Supplementary Fig. 2c). This decreasing shortwave transmissivity imposes a decrease of shortwave radiation at the surface by $-0.09 \pm 0.02\ \mathrm{W\ m^{-2}}$ per decade ($S(1-\alpha)\Delta\tau$; $p < 0.001$, Fig. 1b). On the other hand, the increase in water vapour leads to an increase in atmospheric air emissivity ($3.9 \pm 0.7 \times 10^{-4}$ per decade, $p < 0.001$; Supplementary Fig. 2d), resulting in an increase of downwelling longwave radiation by $0.14 \pm 0.02\ \mathrm{W\ m^{-2}}$ per decade ($\varepsilon_s \sigma T_a^4 \Delta\varepsilon_a$; Fig. 1b).

The radiative forcing associated with the greening-induced changes in α, E, τ, ε_a and r_a totals $-0.24 \pm 0.05\ \mathrm{W\ m^{-2}}$ per decade (Fig. 1b). This radiative forcing leads to a cooling of T_a at a rate of $-0.017 \pm 0.004\ ^\circ\mathrm{C}$ per decade (Supplementary Fig. 3) that is less negative than the trend of T_a from the simulations ($-0.030 \pm 0.006\ ^\circ\mathrm{C}$ per decade; Fig. 1a). The residual reflects the effect of the greening-induced circulation change on T_a (that is, ΔT_a^{cir} in equation (1)). As the cooling effect is dominated by the increasing evapotranspiration, and consequently decreasing shortwave transmissivity, we conclude that the greening mitigates the Earth's climate mainly through its influence on the terrestrial hydrological cycle, particularly through land-surface evapotranspiration[2,12,22].

Spatially, the global cooling effect is primarily contributed by the regions where LAI has increased (Fig. 2). Positive ΔLAI has been attributed in ref. 6 to warming and longer growing seasons over high latitudes, to afforestation and forest management in southeast China, Europe and the eastern United States, and to the CO_2 fertilization effect in the tropics, with substantial uncertainties; meanwhile, due to the deforestation, negative ΔLAI could be also found in some tropical regions (Fig. 2b). In tropical regions, including northwest Amazonia, the Sahel and India, LAI has overall increased at a rate of $0.05 \pm 0.02\ \mathrm{m^2\ m^{-2}}$ per decade ($p < 0.01$), leading to a significant decrease of T_a ($-0.023 \pm 0.007\ ^\circ\mathrm{C}$ per decade, $p < 0.01$). In temperate regions, primarily Europe and southern Siberia, the pronounced greening is simulated to strongly decrease T_a (Fig. 2a). In boreal Eurasia, the greening is modelled to cool T_a, which is at odds with the 'boreal afforestation warming' suggested by previous idealized studies[4,14,23,24]. This discrepancy can be attributed to the difference in the occurrence of seasonal greening as observed and the uniform greening from boreal afforestation. The warming of boreal afforestation is largely attributed to a strong decrease of surface albedo over the winter and early spring seasons through its effect on snow cover[4,14,23,24]. However, the observed greening over the past three decades occurs during the growing season[6,7] (Supplementary Fig. 4), when the snow-albedo feedbacks are minimal. This is also supported by the recent satellite-based studies that found boreal afforestation had a cooling role during the growing season[2].

It is interesting to note that the significantly and strongly increasing LAI in eastern North America and East Asia (Fig. 2b) did not significantly decrease local T_a (Fig. 2a). However, in the second GCM experiment with increasing LAI and climatological SSTs (LAIobs_OCNclim), the increasing LAI did have a significant cooling effect over these two regions (Fig. 2c). Therefore, due to the nonlinearity of the climate system, it is the large-scale atmospheric circulation changes induced by interannual SST and LAI variations in experiment (1) that have masked the local vegetation feedbacks in these regions[25].

To better understand the factors driving changes in T_a due to ΔLAI, we analysed the spatial patterns of trends in α, E, τ, ε_a and r_a resulting from experiment (1) (that is, difference between LAIobs_OCNobs and LAIclim_OCNobs). In most pixels that showed significantly increasing LAI (Fig. 2b), E (91% of pixels), ε_a (88%) and r_a (77%) also increased, whereas α (71%) and τ (75%) decreased (Supplementary Fig. 5). Using equation (1)

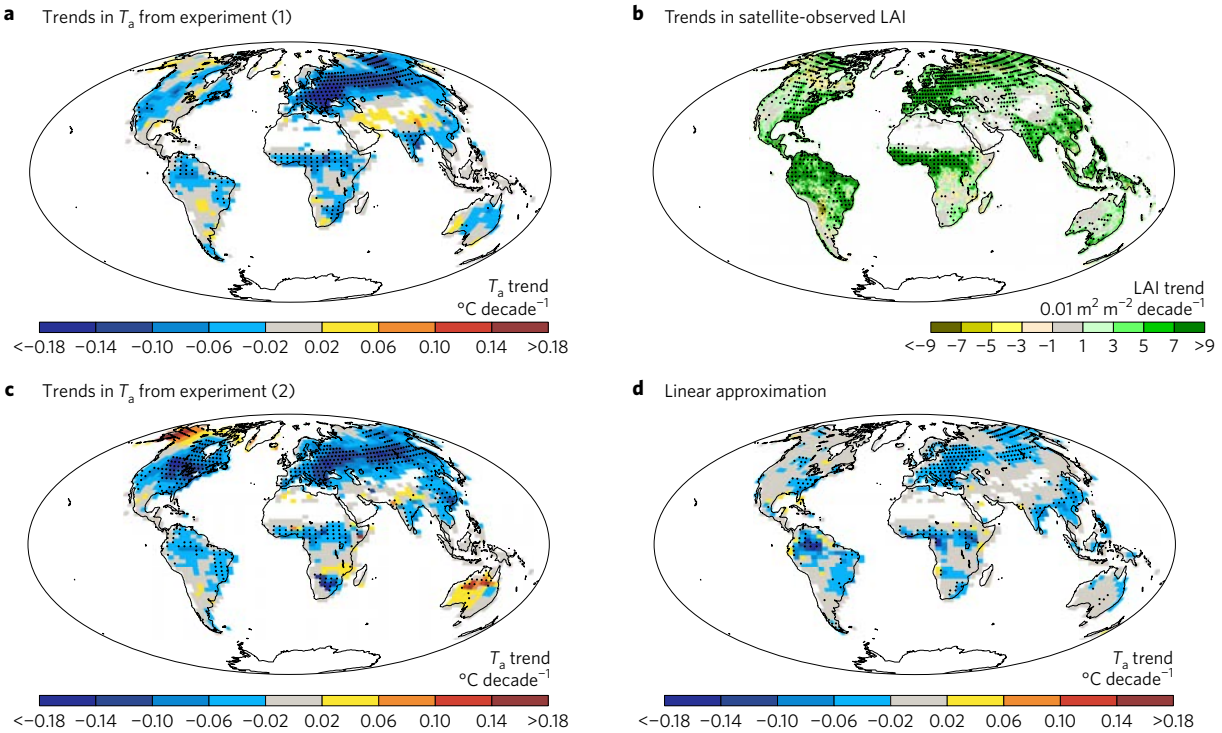

Figure 2 - Patterns of LAI trend and ΔLAI-induced trends in land-surface air temperature (T_a). **a**, ΔLAI-induced trends in T_a from experiment (1) (that is, the trend in LAIobs_OCNobs—LAIclim_OCNobs). **b**, LAI trends derived from satellite observations between 1982 and 2011. **c**, ΔLAI-induced trends in T_a from experiment (2) (that is, the trend in LAIobs_OCNclim). **d**, Trends in T_a due to the ΔLAI-induced radiative forcing from experiment (1) (that is, $(1/f)(-S\tau\Delta\alpha - \lambda\Delta E + S(1-\alpha)\Delta\tau + \varepsilon_s\sigma T_a^4\Delta\varepsilon_a + ((\rho C_d(T_s - T_a))/r_a^2)\Delta r_a)$). Stippling indicates a significant trend (P<0.05).

(but neglecting the influence of atmospheric circulation), we can convert the changes in these variables into the trend in surface radiative forcing (Supplementary Fig. 6) and then the trend in T_a (Fig. 2d), explaining more than half of the simulated negative trend of T_a due to the greening (Fig. 2a). Similar patterns were also found in experiment (2) (Supplementary Fig. 7).

Last, but not least, we found that the simulated sensitivities of evapotranspiration and surface albedo to increasing LAI are within the range of sensitivities from satellite-derived observations (Fig. 3a; see Methods). However, there are large uncertainties in the observed sensitivities. To investigate the influence of different sensitivities, we calibrated the changes in evapotranspiration and surface albedo in equation (1) combined with the observed sensitivities and the climatological values of f, S and τ from the CTRL ensemble simulations (see Methods). We found that the T_a trend ranges from −0.041 to −0.012 °C per decade, resulting from uncertainties in different observational datasets, with an average of −0.029 ± 0.012 °C per decade which is close to the simulated trend (Fig. 3b). To further verify the robustness of our results, we also performed experiments with the Accelerated Climate Modeling for Energy (ACME) branched from the Community Earth System Model (CESM) from the Department of Energy[26] and the Australian Community Climate and Earth System Simulator coupled model (ACCESS) from the Commonwealth Scientific and Industrial Research Organisation[27] following an identical simulation protocol to that used for the IPSL model (Supplementary Text 2). In the ACME and ACCESS GCMs, the modelled T_a changes did not correlate with prescribed LAI (Supplementary Fig. 8). We found that although the modelled evapotranspiration has the same magnitude as the observations, the modelled proportion of transpiration to terrestrial evapotranspiration (T/ET) in both models is seriously underestimated (ref. 28; Supplementary Fig. 9). This underestimation of transpiration naturally leads to very low sensitivities of modelled evapotranspiration to the prescribed increase of LAI (Supplementary Fig. 10a). When the T/ET values

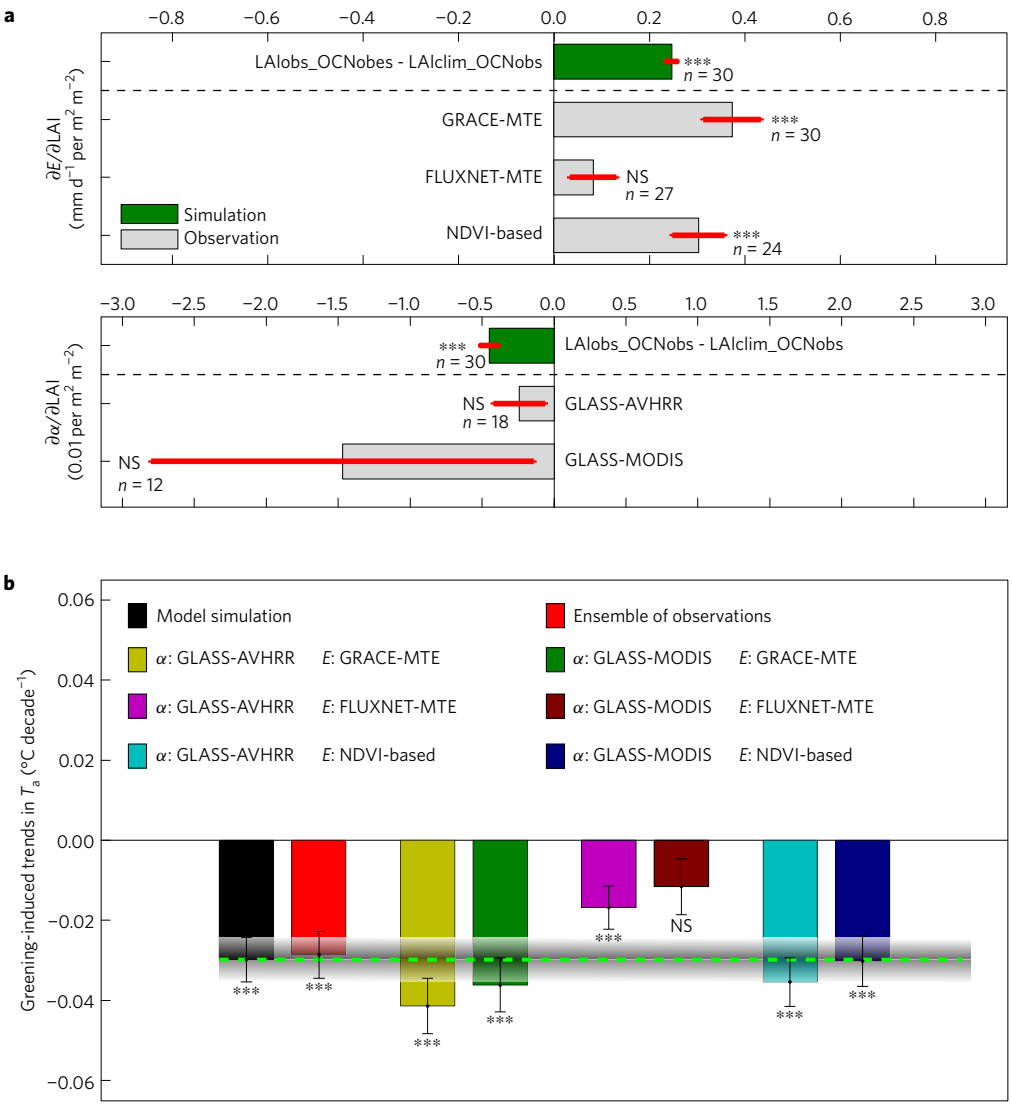

Figure 3 - Sensitivities of evapotranspiration (*E*) and surface albedo (α) to LAI and ΔLAI-induced trends in land-surface air temperature (T_a) calibrated with the observed sensitivities. a, reen Ā bars show the sensitivities from experiment (1), and grey bars show the sensitivities estimated from dierent Ā observations. Number, *n*, is number of years of each dataset used to estimate the sensitivity. Error bars show the standard error of the sensitivity. **b**, ΔLAI-induced trends in T_a calibrated with the combinations of dierent Āobserved sensitivities of surface albedo (α: GLASS-AVHRR, GLASS-MODIS) and evapotranspiration (*E*: GRACE-MTE, FLUXNET-MTE, NDVI-based). The black bar and the horiontal Ādashed green line is the ΔLAI-induced trend in T_a from experiment (1), with one standard error of the trend shown as shadow. The red bar is the ensemble of the ΔLAI-induced trends in T_a calibrated with the combinations. The significances of sensitivity and trend are as follows: ***Significance at the 99% confidence interval; **Significance at the 95%confidence interval; *Significance at the 90% confidence interval; NS, not significant.

are calibrated to be comparable with values suggested by ref. 28 (see methods and Supplementary Text 4), the sensitivities of modelled evapotranspiration to LAI in both models are within the range of the sensitivity values estimated by satellite-derived observations (Supplementary Fig. 10b). Then, we applied equation (1) to calculate the ΔLAI-induced variation in T_a using the calibrated evapotranspiration change (ΔE^{cali}), the modelled $\Delta\alpha$, $\Delta\tau$, $\Delta\varepsilon_a$ and Δr_a, and the climatology of f, S, τ, α, T_s, T_a and r_a from the corresponding models, neglecting the influence of atmospheric circulation changes. For both models, we obtain significant correlations between T_a and LAI ($R = -0.97$ for ACME, $R = -0.88$ for ACCESS, both with $p < 0.001$); the variation of LAI leads to a cooling of $-0.024\,^{\circ}C$ per decade in ACME, and of $-0.052\,^{\circ}C$ per decade in ACCESS (Supplementary Fig. 11), which are consistent with the results from the IPSL model.

In summary, we conclude that the greening-induced biophysical feedbacks have cooled land-surface air temperature. By prescribing the model with the observed LAI and SSTs to provide trustworthy decadal climate simulations, we have not isolated the signature of greening on air temperature over ocean, which calls for further studies. We found that the observed greening partly mitigated the warming induced by rising greenhouse gases, primarily through increased evapotranspiration. We emphasize the importance of model calibration to realistically simulate transpiration processes and biophysical feedbacks. This work highlights the importance of the biophysical feedbacks in the climate system, and the potential of greening to mitigate climate change. As all the Earth System Models used for IPCC AR5 project an optimistic and large increase of LAI in the twenty-first century[9], we expect these negative feedbacks from vegetation to continue. Considering that the biophysical feedback is dominant over regions where vegetation has changed, results from this study have significant implications for future projections of regional climate change. This is of greatest significance to adaptation and mitigation, as policymakers primarily focus on national to sub-national scale interventions. Examples of policy-relevant, region-specific findings from this study include potential mitigation of Europe's increasing heat waves[29], and reduction of the deleterious impacts of warming on tropical crop water use and productivity[3,25,30].

References

1. Myhre, G. D. *et al*. in *Climate Change 2013: The Physical Science Basis* (eds Stocker, T. F. *et al*.) 659–740 (IPCC, Cambridge Univ. Press, 2013).
2. Alkama, R. & Cescatti, A. Biophysical climate impacts of recent changes in global forest cover. *Science* **351,** 600–604 (2016).
3. Mahmood, R. *et al*. Land cover changes and their biogeophysical effects on climate. *Int. J. Climatol.* **34,** 929–953 (2014).
4. Bonan, G. B. Forests and climate change: forcings, feedbacks, and the climate benefits of forests. *Science* **320,** 1444–1449 (2008).
5. Lee, X. H. *et al*. Observed increase in local cooling effect of deforestation at higher latitudes. *Nature* **479,** 384–387 (2011).
6. Zhu, Z. *et al*. Greening of the Earth and its drivers. *Nat. Clim. Change* **6,** 791–795 (2016).
7. Zhu, Z. *et al*. Global data sets of vegetation leaf area index (LAI) 3g and Fraction of Photosynthetically Active Radiation (FPAR) 3g derived from Global Inventory Modeling and Mapping Studies (GIMMS) Normalized Difference Vegetation Index (NDVI3g) for the period 1981 to 2011. *Remote Sens.* **5,** 927–948 (2013).
8. Pan, Y. *et al*. A large and persistent carbon sink in the world's forests. *Science* **333,** 988–993 (2011).
9. Mahowald, N. *et al*. Leaf area index in Earth System Models: evaluation and projections. *Earth Syst. Dyn. Discuss.* **6,** 761–818 (2015).
10. Graven, H. D. *et al*. Enhanced seasonal exchange of CO_2 by Northern ecosystems since 1960. *Science* **341,** 1085–1089 (2013).
11. Canadell, J. G. & Raupach, M. R. Managing forests for climate change mitigation. *Science* **320,** 1456–1457 (2008).
12. Shukla, J. & Mintz, Y. Influence of land-surface evapotranspiration on the Earth's climate. *Science* **215,** 1498–1501 (1982).
13. Shen, M. *et al*. Evaporative cooling over the Tibetan Plateau induced by vegetation growth. *Proc. Natl Acad. Sci. USA* **112,** 9299–9304 (2015).
14. Betts, R. A. Offset of the potential carbon sink from boreal forestation by decreases in surface albedo. *Nature* **408,** 187–190 (2000).
15. Jackson, R. B. *et al*. Protecting climate with forests. *Environ. Res. Lett.* **3,** 044006 (2008).
16. Kala, J. *et al*. Influence of leaf area index prescriptions on simulations of heat, moisture, and carbon fluxes. *J. Hydrometeorol.* **15,** 489–503 (2013).
17. Wang, J. *et al*. Impact of deforestation in the Amazon basin on cloud climatology. *Proc. Natl Acad. Sci. USA* **106,** 3670–3674 (2009).
18. Swann, A. L. S., Fung, I. Y. & Chiang, J. C. H. Mid-latitude afforestation shifts general circulation and tropical precipitation. *Proc. Natl Acad. Sci. USA* **109,** 712–716 (2012).
19. Marti, O. *et al*. Key features of the IPSL ocean atmosphere model and its sensitivity to atmospheric resolution. *Clim. Dyn.* **34,** 1–26 (2010).
20. Hartmann, D. L. *et al*. in *Climate Change 2013: The Physical Science Basis* (eds Stocker, T. F. *et al*.) 159–254 (IPCC, Cambridge Univ. Press, 2013).
21. Voigt, A. & Shaw, T. A. Circulation response to warming shaped by radiative changes of clouds and water vapour. *Nat. Geosci.* **8,** 102–106 (2015).
22. Chahine, M. T. The hydrological cycle and its influence on climate. *Nature* **359,** 373–380 (1992).
23. Levis, S., Foley, J. & Pollard, D. Potential high-latitude vegetation feedbacks on CO_2-induced climate change. *Geophys. Res. Lett.* **26,** 747–750 (1999).
24. Bala, G. *et al*. Combined climate and carbon-cycle effects of large-scale deforestation. *Proc. Natl Acad. Sci. USA* **104,** 6550–6555 (2007).
25. Lawrence, D. & Vandecar, K. Effects of tropical deforestation on climate and agriculture. *Nat. Clim. Change* **5,** 27–36 (2015).
26. Small, J. *et al*. A new synoptic scale resolving global climate simulation using the Community Earth System model. *J. Adv. Model. Earth Syst.* **6,** 1065–1094 (2014).
27. Bi, D. *et al*. The ACCESS coupled model: description, control climate and evaluation. *Aust. Meteorol. Oceanogr. J.* **63,** 41–64 (2013).
28. Good, S. P., Noone, D. & Bowen, G. Hydrologic connectivity constrains partitioning of global terrestrial water fluxes. *Science* **349,** 175–177 (2015).
29. Ciais, P. *et al*. Europe-wide reduction in primary productivity caused by the heat and drought in 2003. *Nature* **437,** 529–533 (2005).
30. Lyndon, D. E. *et al*. Changing water availability during the African maize-growing season, 1979–2010. *Environ. Res. Lett.* **9,** 075005 (2014).

Acknowledgements

This study was supported by the National Natural Science Foundation of China (41530528 and 41561134016), National Youth Top-notch Talent Support Program in China, and the 111 Project (B14001). We thank the National Supercomputer Center in Tianjin, China (NSCC-TJ), the National Computer Center IDRIS of CNRS in France, the Commonwealth Scientific and Industrial Research Organisation in Australia, and the Oak Ridge National Laboratory in the United States for providing computing resources. J.M. is supported by the Biogeochemistry-Climate Feedbacks Scientific Focus Area project and the project under contract of DE-SC0012534 funded through the Regional and Global Climate Modeling Program, and the Terrestrial Ecosystem Science Scientific Focus Area project funded through the Terrestrial Ecosystem Science Program in the Climate and Environmental Sciences Division (CESD) of the Biological and Environmental Research (BER) Program in the US Department of Energy Office of Science. X.S. is supported by the Accelerated Climate Modeling for Energy project funded through the Earth System Modeling Program in the CESD of the BER Program in the US Department of Energy Office of Science. This research used the resources of the Oak Ridge Leadership Computing Facility at the Oak Ridge National Laboratory, which is supported by the Office of Science of the US Department of Energy under Contact No. DE-AC05-00OR22725.

Author contributions

S.Piao, L.Z.X.L. and Z.Z. designed the research; Z.Z., L.Z.X.L., Y.L., X.S. and J.M. performed the simulations; Z.Z. performed analysis; Z.Z. and S.Piao wrote the draft; and all the authors contributed to the interpretation of the results and the writing of the paper.

Methods

Forcing data sets. The monthly LAI maps from 1982 to 2011 were derived from the Advanced Very High Resolution Radiometer (AVHRR) 8-km global LAI product[7]. We prescribed LAI from each map into each grid square and for each plant functional type, using the Olson land-cover map at 5 km resolution based on the 1-km IGBP map. The monthly maps of sea-surface temperature and sea ice from 1982 to 2011 at a 1° by 1° resolution were obtained from the Atmospheric Model Intercomparison Project (AMIP; http://www-pcmdi.llnl.gov/projects/amip). The data set is derived from observations, and is recommended for use in AMIP simulations.

Model and experiments. To reduce the uncertainties in the GCM simulations associated with systematic SST biases in fully coupled Earth System Models[31,32], we used the AMIP-type simulation strategy and thus ignored the ocean coupling by prescribing SSTs. We used the IPSLCM (version 4) coupled land–atmosphere model[19] from the Institute Pierre Simon Laplace (IPSL) modelling community to simulate the climate effects of the increasing LAI during the past three decades. The atmospheric component of the model is the Laboratoire de Météorologie Dynamique atmospheric general circulation model with zooming capability (LMDZ; refs 33,34), which is coupled with the land-surface model Organising Carbon and Hydrology In Dynamic Ecosystems (ORCHIDEE; ref. 35). ORCHIDEE has performances comparable to other land-surface models and diagnostic datasets in simulating land evapotranspiration[36] and soil moisture[37]. The land-surface model was modified to replace modelled LAI with satellite-observed values.

To document internal variability of the coupled land–atmosphere system, we first performed a control experiment (CTRL), consisting of a set of thirty realizations of 30 years each. The lower boundary conditions are mean SSTs and LAI averaged for the period from 1982 to 2011. The 30 realizations started with different initial conditions. The unforced land–atmosphere system has a large internal variability (grey lines in Supplementary Fig. 12), defined as noise[38,39]. The noise, calculated as the standard deviation of annual global land-surface (at 2 metres) air temperature, equals 0.12 °C across all simulation years ($n=900$) in CTRL even though both SSTs and LAI were fixed. We then analysed the average of the 30 simulations, defined as the ensemble mean. The ensemble mean does not show significant trends ($p>0.1$) and presents a very small interannual standard deviation of T_a in CTRL (the black line in Supplementary Fig. 12), showing that the internal variability due to initial conditions is mainly of random type. Thus, to reduce this random uncertainty in a climate simulation due to initial conditions[38], each experiment in this study comprises a 30-member ensemble of transient climate simulations with different initial conditions (initial-condition ensemble) and the average of simulations (ensemble average) is analysed to highlight the forced signal due to the greening.

To separate vegetation biophysical feedbacks on climate from internal climate variability, we designed two climate experiments with different forcing of LAI and SSTs (see Supplementary Table 1) for the period from 1982 to 2011. The inclusion of interannual variations of historical LAI and SSTs in LAIobs_OCNobs reproduces the observed interannual variations of T_a ($R=0.84$, $p<0.001$; Supplementary Fig. 13)[31,40]. In experiment (1), the differences between LAIobs_OCNobs and LAIclim_OCNobs isolate the ΔLAI-induced climate effects. Experiment (2) (that is, LAIobs_OCNclim) is complementary because it does not consider the historical SST variations modulating the LAI effects on climate, and thus allows us to isolate the fingerprint of observed LAI changes on climate. The differences between experiment (1) and experiment (2) are due to the effect of SST-induced circulation changes on the biophysical vegetation–climate feedbacks.

The 30-member ensemble of transient simulations is resource-intensive, totalling 43,200 months of simulations. The resolution of the model applied in this study was 2.5° latitude × 3.75° longitude, with 19 levels in the vertical and a 3-minute time step. The initial conditions are the outputs of the past 30 years from a long-term spin-up simulation. Greenhouse gases (for example, CO_2, CH_4, N_2O) and aerosols are prescribed based on their typical climatological values in the model to isolate the LAI effects on climate changes. The analysis did not include those model grids with multiyear (1982–2011) average LAI < 0.1. The IPSLCM GCM was run at the National Computer Center IDRIS in France. In this study, we force the GCM only with the satellite-observed year-to-year LAI to isolate the climate effect of greening from other confounding forcings. Doing so ignores the potential effects of rising CO_2 on the LAI–climate feedbacks. Nevertheless, we performed three additional 60-year-long simulations to estimate this effect. The results show that rising atmospheric CO_2 does not change the LAI–climate feedbacks, as the reduction of evapotranspiration due to the physiological effect of rising CO_2 is mostly cancelled out by the increase of evapotranspiration due to the radiative effect of rising CO_2 (details see Supplementary Text 1).

To further estimate the uncertainty associated with model structures, we wrote a simulation protocol and performed more model simulations following the protocol to investigate the climate effects of Earth greening. We also performed experiments with the Accelerated Climate Modeling for Energy (ACME) from the Department of Energy[26] and the Australian Community Climate and Earth System Simulator coupled model (ACCESS) from the Commonwealth Scientific and Industrial Research Organisation[27] following an identical simulation protocol to that used for the IPSL model to verify the robustness of our results. ACME and ACCESS were ran exactly following the simulation protocol as used for IPSLCM (details see Supplementary Text 2–4).

Decomposition of LAI–climate feedbacks into separate mechanisms. The surface energy balance controls land–atmosphere interactions. As shown in Supplementary Fig. 14, there are two dominant factors in driving the changes of land-surface 2-m air temperature (T_a): first, the radiative and thermodynamic variations of land surface acts directly on land-surface temperature (T_s), the change of T_s interacts on T_a locally through radiative (for example, long wave radiation) and non-radiative (for example, sensible heat) fluxes (ΔT_a^{rad}); second, the change in atmospheric circulation (for example, advection of cold and warm air masses) acts more directly on T_a (ΔT_a^{cir}). That is:

$$\Delta T_a = \Delta T_a^{rad} + \Delta T_a^{cir} \quad (2)$$

We first estimate the change in T_s associated with the ΔLAI-induced radiative and thermodynamic forcings because the land-surface energy budget is calculated at the land-surface layer (Supplementary Fig. 14). The land-surface energy balance is given by:

$$S_n + L_n = \lambda E + H + G \quad (3)$$

where S_n is the net shortwave radiation at the surface, L_n is the net longwave radiation at the surface, λ is the latent heat of vaporization, E is evapotranspiration, H is the sensible heat flux and G is the ground heat flux, which can be neglected due to its small magnitude on seasonal and longer timescales (Supplementary Table 2). Equation (3) can be rewritten as:

$$S_n - \lambda E = H - L_n \quad (4)$$

where vegetation dynamics directly modify the two left-hand terms via albedo and evapotranspiration, and imposes a LAI-induced forcing (disequilibrium of energy); the right-hand terms are functions of T_a and T_s, and represent the fact that the coupled land–atmosphere system adjusts T_a and T_s to keep the surface energy in balance locally.

S_n, L_n, λE and H are given as:

$$S_n = S\tau(1-\alpha) \quad (5)$$

where S is the solar radiation flux at the top of atmosphere, τ is the atmospheric shortwave transmissivity, α is the surface albedo. The variation of τ, depending on changes in atmospheric water vapour and clouds, is calculated from the GCM values. Increasing LAI thus influences α directly, and τ indirectly, through LAI-related changes in cloud cover and atmospheric water vapour content.

As most of atmospheric water vapour is confined near the surface, some empirical equations can provide very good estimates of downward longwave radiation worldwide using surface observations[41]. In this study, the GCM-simulated T_a at 2 m height was used in the bulk formula (see Supplementary Fig. 14). According to the Stephan–Boltzmann law, given atmospheric air emissivity (ε_a), the downward longwave radiation at the land surface can be estimated roughly as

$$L_\downarrow = \varepsilon_a \sigma T_a^4 \quad (6)$$

where σ is the Stephan–Boltzmann constant and T_a is the near-surface air temperature. σ equals 5.67×10^{-8} W m^{-2} K^{-4}. Similar to τ, ε_a is also calculated from the GCM values and its variation is driven by changes in atmospheric water vapour and clouds.

The upward longwave radiation is given by

$$L_\uparrow = (1-\varepsilon_s)\varepsilon_a \sigma T_a^4 + \varepsilon_s \sigma T_s^4 \quad (7)$$

where ε_s is the land-surface emissivity. Note the land-surface emissivity (ε_s) also changes with land cover, soil moisture and snow cover. Here we treat it as a constant of 0.95 for simplicity, as satellite-observed surface emissivity varies little over mostly vegetated surfaces and changes only slightly from 0.95 among different land covers[42]. Thus, the net longwave radiation over the land surface is given by

$$L_n = L_\downarrow - L_\uparrow = \varepsilon_s \sigma (\varepsilon_a T_a^4 - T_s^4) \quad (8)$$

The latent heat can be written as:

$$\lambda E = \lambda \beta E_P \quad (9)$$

where E_P is the potential evapotranspiration and β is a diagnostic parameter ($0 \le \beta \le 1$) related to all mechanisms through which actual E is below the potential rate (E_P). The ORCHIDEE parameterizations to calculate E are fairly complex[35]

and they are replaced here by the simple diagnostic parameter β. LAI directly influences β through aerodynamic conductance (part of the canopy conductance) and also indirectly through stomatal conductance, because in ORCHIDEE the stomatal conductance per unit leaf area depends on the near-surface atmospheric humidity, impacted by LAI feedbacks on the atmosphere.

The sensible heat flux is given by:

$$H = \rho C_d \frac{T_s - T_a}{r_a} \tag{10}$$

where ρ is the air density, C_d is the specific heat of air at constant pressure and r_a is the aerodynamic resistance at 2 m height. ρ is equal to 1.21 kg m^{-3}; C_d to 1,013 J kg^{-1} K^{-1}. In this study, the change in r_a is derived from the LAI-induced change in surface roughness, but does not consider the effect of changing vegetation structure (height, clumping) and changing vegetation density on the surface roughness.

Making use of equations (3)–(10), the surface energy balance equation is expanded into the following form:

$$S\tau(1-\alpha) - \lambda E = \rho C_d \frac{T_s - T_a}{r_a} - \varepsilon_s \sigma (\varepsilon_a T_a^4 - T_s^4) \tag{11}$$

Assuming that S, λ, ρ, C_d, σ and ε_s are independent of T_s, we further differentiate the equation (11) with respect to T_s, giving the change ΔT_s:

$$\Delta T_s = \frac{1}{f_s}\left(-S\tau\Delta\alpha - \lambda\Delta E + S(1-\alpha)\Delta\tau + \varepsilon_s\sigma T_a^4 \Delta\varepsilon_a + \frac{\rho C_d (T_s - T_a)}{r_a^2}\Delta r_a \right) + \frac{\rho C_d / r_a + 4\varepsilon_s\sigma\varepsilon_a T_a^3}{\rho C_d / r_a + 4\varepsilon_s\sigma T_s^3}\Delta T_a \tag{12}$$

where f_s is an energy redistribution factor, given by:

$$f_s = \rho C_d / r_a + 4\varepsilon_s \sigma T_s^3 \tag{13}$$

f_s^{-1} represents the land-surface temperature sensitivity to 1 W m^{-2} radiative forcing at the land surface.

On the right-hand side of equation (12), the first term represents the land-surface temperature change due to radiative and thermodynamic forcings associated with LAI-caused changes in surface albedo, evapotranspiration, shortwave transmissivity, air emissivity and aerodynamic resistance ($\Delta T_s^{rad} = (1/f)(-S\tau\Delta\alpha - \lambda\Delta E + S(1-\alpha)\Delta\tau + \varepsilon_s\sigma T_a^4\Delta\varepsilon_a + ((\rho C_d(T_s - T_a))/(r_a^2))\Delta r_a)$). The second term $(((\rho C_d/r_a + 4\varepsilon_s\sigma\varepsilon_a T_a^3)/(\rho C_d/r_a + 4\varepsilon_s\sigma T_s^3))\Delta T_a)$ quantifies the strong coupling between T_a and T_s (Supplementary Fig. 14). On the one hand, it reveals that T_s varies with T_a due to ΔLAI-induced change in air advection, such as the LAI-perturbed advection of cold and warm air masses ($\Delta T_s^{cir} = ((\rho C_d/r_a + 4\varepsilon_s\sigma\varepsilon_a T_a^3)/(\rho C_d/r_a + 4\varepsilon_s\sigma T_s^3))\Delta T_a^{cir}$). On the other hand, it also shows that the change in T_s further drives a change in T_a via the change in surface heating rate ($\Delta T_a^{rad} = ((\rho C_d/r_a + 4\varepsilon_s\sigma T_s^3)/(\rho C_d/r_a + 4\varepsilon_s\sigma\varepsilon_a T_a^3))\Delta T_s^{rad}$). Using equations (2) and (12) leads us to the derivation of equation (1) in the main text:

$$\Delta T_a = \frac{1}{f}\left(-S\tau\Delta\alpha - \lambda\Delta E + S(1-\alpha)\Delta\tau + \varepsilon_s\sigma T_a^4\Delta\varepsilon_a + \frac{\rho C_d (T_s - T_a)}{r_a^2}\Delta r_a \right) + \Delta T_a^{cir} \tag{14}$$

where f is:

$$f = \rho C_d / r_a + 4\varepsilon_s\sigma\varepsilon_a T_a^3 \tag{15}$$

f^{-1} represents the land-surface air temperature sensitivity to 1 W m^{-2} radiative forcing at the land surface. The climatology of f is diagnosed from the multiyear average of the ensemble simulations of each GCM (the CTRL ensemble simulations by IPSLCM, the S1 ensemble simulations by ACME and ACCESS).

Observation-based estimate of the sensitivities of evapotranspiration and surface albedo to increasing LAI. We use the three long-term global evapotranspiration products, namely GRACE-MTE (1982–2009, based on the water balance of different catchments[43]), FLUXNET-MTE (1982–2008, based on surface flux measurements[44]) and an NDVI-based data set (1983–2006, based on satellite-derived Normalized Difference Vegetation Index[45]). The long-term global land-surface albedo product is from the GLASS dataset[46], which is generated from satellite observations and available from 1982 to 2011. The GLASS albedo product is derived from AVHRR data from 1982 to 1999, and then from MODIS data from 2000 to 2011. This discontinuity results in an irrational positive sensitivity of surface albedo to LAI during the whole study period (1982–2011). We thus estimated the sensitivity of surface albedo to LAI, separating the GLASS data set into two periods: 1982–1999 (GLASS-AVHRR) and 2000–2011 (GLASS-MODIS). As the GLASS albedo product is self-consistent with the MODIS albedo product[46], we did not repeatedly show the sensitivity from the MODIS albedo product. The observed sensitivity of land evapotranspiration to LAI ($\partial E/\partial$LAI) is estimated based on the regression: $E = k_1 \mathrm{LAI} + k_2 P + k_3 T_a + k_4$, where P and T_a are the observed annual land precipitation and land-surface air temperature for 1982–2011 from the CRU data set[47]; k_1 is the estimated $\partial E/\partial$LAI controlling P and T_a. Similarly, the observed sensitivity of land-surface albedo to increasing LAI ($\partial\alpha/\partial$LAI) is estimated based on the regression: $\alpha = k_1 \mathrm{LAI} + k_2 C_{snow} + k_3$, where C_{snow} is the observed annual land snow cover from NASA DAAC at the National Snow & Ice Data Center[48]; k_1 is the estimated $\partial\alpha/\partial$LAI controlling snow cover.

Calibration of temperature change from GCMs based on observation-based sensitivities. Using the climatology of S, τ, α, T_s, T_a, r_a and f from the CTRL GCM simulation, the changes of surface albedo, evapotranspiration, shortwave transmissivity, air emissivity and aerodynamic resistance lead to a trend of land-surface air temperature via equation (1) in the main text.

The observation-based sensitivities of evapotranspiration and surface albedo can be substituted in equation (1) of the main text to calibrate the modelled greening-induced change in T_a. We assume the same spatial patterns of ΔLAI-induced changes in evapotranspiration (ΔE) and surface albedo ($\Delta\alpha$) as the patterns in the GCM experiment (1). Then, we substitute the observed sensitivities by multiplied ΔE ($\Delta\alpha$) with λ_E (λ_α) in each pixel, where λ_E (λ_α) is the ratio between the observation-derived sensitivity (see above) and the GCM-simulated sensitivity, respectively. The calibrated greening-induced change in surface air temperature (ΔT_a^{cali}) is obtained by

$$\Delta T_a^{cali} = \Delta T_a^{mod} + \frac{-S\tau\Delta\alpha}{f}(\lambda_\alpha - 1) + \frac{-\lambda\Delta E}{f}(\lambda_E - 1) \tag{16}$$

where ΔT_a^{mod} is the modelled greening-induced change in T_a from equation (1) in the main text. Note that we have not calibrated the greening-induced changes in shortwave transmissivity, air emissivity, aerodynamic resistance and circulations due to the lack of observations, and thus used GCM results for these quantities.

Code availability. IPSLCM GCM model code is available at http://forge.ipsl.jussieu.fr/igcmg/svn/modipsl/trunk. The program used to generate all the results is MATLAB. Analysis scripts are available by request to S.Piao.

Data availability. The satellite-observed LAI3g data sets are available from the NASA Earth Exchange (NEX) web site (https://nex.nasa.gov/nex). The AMIP SST and sea ice boundary conditions are available at http://www-pcmdi.llnl.gov/projects/amip. Model outputs are available on request from S.Piao.

References

31. Kosaka, Y. & Xie, S. P. Recent global-warming hiatus tied to equatorial Pacific surface cooling. *Nature* **501,** 403–407 (2013).
32. He, J. & Soden, B. J. The impact of SST biases on projections of anthropogenic climate change: a greater role for atmosphere-only models? *Geophys. Res. Lett.* **43,** 7745–7750 (2016).
33. Li, Z. X. Ensemble atmospheric GCM simulation of climate interannual variability from 1979 to 1994. *J. Clim.* **12,** 986–1001 (1999).
34. Hourdin, F. *et al*. The LMDZ4 general circulation model: climate performance and sensitivity to parametrized physics with emphasis on tropical convection. *Clim. Dyn.* **27,** 787–813 (2006).
35. Krinner, G. *et al*. A dynamic global vegetation model for studies of the coupled atmosphere-biosphere system. *Glob. Biogeochem. Cycles* **19,** GB1015 (2005).
36. Mueller, B. & Seneviratne, S. I. Systematic land climate and evapotranspiration biases in CMIP5 simulations. *Geophys. Res. Lett.* **41,** 128–134 (2014).
37. Rebel, K. T. *et al*. A global analysis of soil moisture derived from satellite observations and a land surface model. *Hydrol. Earth Syst. Sci.* **16,** 833–847 (2012).
38. Lorenz, E. N. Deterministic nonperiodic flow. *J. Atmos. Sci.* **20,** 130–141 (1963).
39. Lombardozzi, D., Bonan, G. B. & Nychka, D. W. The emerging anthropogenic signal in land-atmosphere carbon-cycle coupling. *Nat. Clim. Change* **4,** 796–800 (2014).
40. Compo, G. & Sardeshmukh, P. Oceanic influences on recent continental warming. *Clim. Dyn.* **32,** 333–342 (2009).
41. Wang, K. & Liang, S. Global atmospheric downward longwave radiation over land surface under all-sky conditions from 1973 to 2008. *J. Geophys. Res.* **114,** D19101 (2009).
42. Zhou, L. *et al*. Asymmetric response of maximum and minimum temperatures to soil emissivity change over the Northern African Sahel in a GCM. *Geophys. Res. Lett.* **35,** L05402 (2008).

43. Zeng, Z. *et al*. A worldwide analysis of spatiotemporal changes in water balance based evapotranspiration from 1982 to 2009. *J. Geophys. Res.* **119,** 1186–1202 (2014).
44. Jung, M. *et al*. Recent decline in the global land evapotranspiration trend due to limited moisture supply. *Nature* **467,** 951–954 (2010).
45. Zhang, K., Kimball, J. S., Nemani, R. R. & Running, S. W. A continuous satellite-derived global record of land surface evapotranspiration from 1983 to 2006. *Wat. Resour. Res.* **46,** W09522 (2010).
46. Liu, Q. *et al*. Preliminary evaluation of the long-term GLASS albedo product. *Int. J. Digit. Earth* **6,** 69–95 (2013).
47. Harris, I., Jones, P. D., Osborn, T. J. & Lister, D. H. Updated high-resolution grids of monthly climatic observations—the CRU TS3.10 Dataset. *Int. J. Climatol.* **34,** 623–642 (2014).
48. Brodzik, M. & Armstrong, R. *Northern Hemisphere EASE-Grid 2.0 Weekly Snow Cover and Sea Ice Extent. Version 4* (NASA DAAC at the National Snow and Ice Data Center, 2013).